Competition between different long-distance superexchange couplings in a quadripartite spin-crossover molecular device

Zhi-Hong Yuan, Jun Zhang, Yong-Chen Xiong,* Wang-Huai Zhou,† Nan Nan, and Xin-Ke Li

Shiyan Key Laboratory of Quantum Information and Precision Optics, and School of Mathematics, Physics and Optoelectronic Engineering, Hubei University of Automotive Technology, Shiyan 442002, People's Republic of China;

Hubei Key Laboratory of Energy Storage and Power Battery, and Collaborative Innovation Center for Optoelectronic Technology, Hubei University of Automotive Technology, Shiyan 442002, People's Republic of China;

and Institute of Shiyan Industrial Technology of Chinese Academy of Engineering, Shiyan 442002, People's Republic of China

(Received 4 December 2023; revised 29 January 2024; accepted 4 March 2024; published 18 March 2024)

Long-distance superexchange coupling provides a powerful tool for scalable quantum processors required in quantum information and quantum computation. Quadripartite spin-crossover molecules are prototypical systems for studying novel quantum phenomena assisted by superexchange interactions. In this paper, we consider a quadripartite molecule where two central monomers are connected to two electrodes, whereas another two are side coupled to their neighboring central monomers. Numerical renormalization group results demonstrate that, when the energy level spacing between two central monomers Δ turns on, spins on the two side monomers are organized ferromagnetically. The effective antiferromagnetic superexchange interaction between the side units and the electrodes then induces a long-distance ferromagnetic Ruderman-Kittel-Kasuya-Yosida interaction between two side monomers. For intermediate Δ, the linear conductance tends to reach its unitary limit in a moderate low-temperature regime due to a superexchange two-stage Kondo effect. When the hopping integral between two central monomers sweeps upwards, where Δ is fixed at a small value, a quantum phase transition occurs. A long-distance antiferromagnetic exchange coupling between two side units is clarified, isolating the molecule from the electrodes with zero conductance. If Δ is set to be an intermediate value, applying the hopping integral then triggers a singular quantum phase, where two central monomers are antiparallelly aligned, whereas two side ones are organized ferromagnetically, revealing well the competition between the above two kinds of long-distance superexchange couplings. Temperature-dependent images and numerical simulations confirm the above conclusions.

DOI: 10.1103/PhysRevB.109.115421

I. INTRODUCTION

Heisenberg exchange interaction plays an important role in many branches of condensed matter physics and related technologies [1,2]. It allows precise voltage control over spin dynamics, due to the ability to control the overlap of orbital wavefunctions [3–5]. This feature ensures the study of fundamental quantum behaviors [6–8] and finds potential applications in quantum information processing [9–12]. However, it is intrinsically short ranged, which fails to meet the requirement of large-scale quantum computing [3,4,13], while long-range interactions between two remote spins may develop due to virtual processes through any mediator quantum system [14]. This mechanism is the so-called superexchange, and is present in various nanoscale structures. Many approaches to implement superexchange coupling between distant quantum systems have been proposed, using a variety of coupling mechanisms. These include an empty [3,15], single-electron [14], multielectron [4,16] or virtually occupied [17] quantum dot. Previous works have suggested that such long-range connectivity may be highly advantageous for quantum error correction [12,18], as well as for reducing the number of operations required in quantum algorithms [14,19], and is also essential for quantum-state transfer in a quantum data bus [20,21]. So far, the effect of long-distance superexchange couplings on the electronic transport is still lacking.

Coupled quadripartite spin chains are prototypical systems predicted to exhibit superexchange couplings, which are important for studying long-distance state transfer and remote entanglement [4,5,21–23]. Distinguishing from such isolated systems, the physical picture may become quite different if the quadripartite spin chain connects to external electrodes, which provides opportunities to reveal the electronic transport properties manipulated by long-distance superexchange couplings. In the present work, we considered a spin chain constituted by a quadripartite spin-crossover molecule (QSCM), where two central units are connected to the source and drain electrodes, whereas the other two units are only side coupled to their neighboring central units, see Fig. 1. Taking the interaction between the electrodes and the central units into account, such an architecture may exhibit various kinds of superexchange couplings. Disclosing the electronic transport property and quantum phase transition (QPT) of such a structure is important both for fundamental reasons, as well as for designing novel quantum devices. Our main findings include the following. When the energy level difference

*xiongyc_lx@huat.edu.cn
†zhouwh@huat.edu.cn

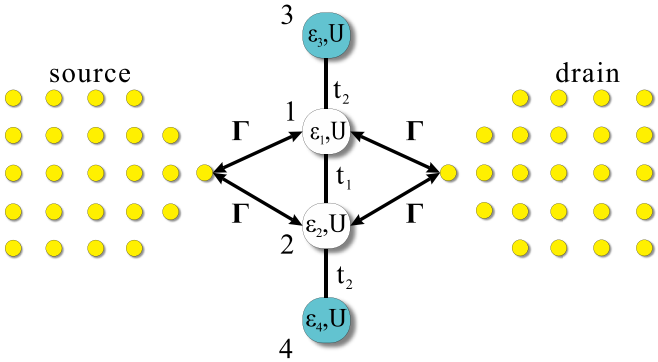

FIG. 1. Schematic illustration of the quadripartite spin-crossover molecule (QSCM) connected to the source (S) and drain (D) electrodes. Molecular monomers (MMs) 1 and 2 connect directly to the electrodes, while each side monomer (MM3 or MM4) only connects with its neighboring central monomer. ϵ_i is the energy level of the ith monomer, U is the on-site electron-electron repulsion, and Γ is the hybridization function between the central monomers and the conduction bands. t_1 illustrates the interorbital hopping integral (tunneling coupling) between the two central monomers, and t_2 is that between the central monomer and its corresponding side unit.

between two central units Δ sweeps upwards, spins on the two side units keep at a ferromagnetic configuration. For small Δ, the origination of the ferromagnetic interaction includes two aspects: the one mediated by the spin triplet of two central units, and that mediated by the antiferromagnetic superexchange interaction between the side units and the electrodes. The latter one is analogous to a Ruderman-Kittel-Kasuya-Yosida (RKKY) interaction mediated by the superexchange interaction. For large Δ, only the latter one contributes to the ferromagnetic configuration, because the side units nearly decouple from their neighboring central units. For intermediate Δ, the linear conductance tends to reach its unitary limit in a moderate low-temperature regime due to a superexchange two-stage Kondo effect. When the hopping integral between two central units is applied, both the spin correlations between two central units and two side units change to antiferromagnetic through a QPT if Δ is fixed at a small value. A long-distance exchange coupling between two side units is clarified, isolating the chain from the electrodes with zero conductance. Temperature-dependent images and numerical simulations confirm the above conclusions. If Δ is fixed at an intermediate value, applying the hopping integral between two central units then triggers a singular quantum phase, where two central monomers are antiparallelly organized, whereas two side ones are aligned ferromagnetically. Superexchange Kondo effect appears at low-enough temperature.

The remaining part of this paper is organized as follows. In Sec. II, we give the many-body Hamiltonian of the QSCM device, and present the calculation method and basic formulas. In Sec. III, we show the numerical results and their discussions. Finally, a conclusion is given.

II. MODEL AND METHOD

To study the quantum behaviors assisted by long-distance superexchange couplings, we consider a QSCM device, with its schematic illustration schematically shown in Fig. 1. In such a device, the molecular monomers 1 and 2 (MM1 and MM2, the central molecular monomers) are connected directly to the source (S) and drain (D) electrodes in a parallel configuration, whereas MM3 and MM4 (the side molecular monomers) have no direct connections to the conduction leads. According to this architecture, we can build the Hamiltonian based on a four impurity Anderson model, which is written as [24–26]

$$H = H_\nu + H_M + H_{hyb}, \tag{1}$$

$$H_\nu = \sum_{\nu k\sigma} \epsilon_{\nu k\sigma} c^\dagger_{\nu k\sigma} c_{\nu k\sigma}, \tag{2}$$

$$\begin{aligned} H_M = &\sum_{i=1}^{4}\sum_{\sigma} \epsilon_i n_{i\sigma} + \sum_{i=1}^{4} U_i n_{i\uparrow} n_{i\downarrow} \\ &- t_1 \sum_{\sigma} (d^\dagger_{1\sigma} d_{2\sigma} + \text{H.c.}) \\ &- t_2 \sum_{\sigma} (d^\dagger_{1\sigma} d_{3\sigma} + d^\dagger_{2\sigma} d_{4\sigma} + \text{H.c.}), \end{aligned} \tag{3}$$

$$H_{hyb} = \sum_{i=1}^{2}\sum_{\nu k\sigma} \tau_{\nu k\sigma} (c^\dagger_{\nu k\sigma} d_{i\sigma} + \text{H.c.}). \tag{4}$$

Here, H_ν ($\nu = S, D$) represents the contribution of the noninteracting metal electrode. $\epsilon_{\nu k\sigma}$ is the electron energy with respect to the Fermi level, where k is the wave vector of the free conduction electrons, and σ is the spin index ($\sigma = \uparrow$ or $\downarrow$). $c^\dagger_{\nu k\sigma}$ ($c_{\nu k\sigma}$) is the creation (annihilation) operator for conduction electrons with spin σ. H_M is the Hamiltonian of the spin-crossover molecule. $n_{i\sigma} = d^\dagger_{i\sigma} d_{i\sigma}$ is the number operator of electrons in MMi ($i = 1, 2, 3, 4$) with energy ϵ_i and spin σ. Experimentally, ϵ_i can be controlled by an external gate voltage V_g [26]. U_i corresponds to the strength of Coulomb repulsion in MMi, t_1 is the hopping integral between two central monomers, and t_2 is that between one side monomer and its neighboring central monomer. To be specific, U_i depends closely on the orbital properties, and results from the fact that if an electron with energy ϵ_i is localized on the transport-active orbital of MMi, a latter one with an antiparallel spin direction injected into the same orbital will have an energy $\epsilon_i + U$. t_i may lead to an antiferromagnetic exchange coupling, and is always determined by the wavefunction overlaps, and hence could be adjusted by the distance of different monomers. For the sake of simplicity, we assume that the repulsions on four monomers are identical, namely, $U_i = U$. Finally, H_{hyb} is the contribution of the hybridization between the conduction band and the central monomers. τ is the tunneling coupling, which is assumed to be source-drain symmetric and k, σ independent, hence we omit its subscript in the following, i.e., $\tau_{\nu k\sigma} \equiv \tau$.

In this paper, we focus on the electronic transport and QPTs of the device in the strongly correlated regime. It is noticed that when electrons in the molecular orbitals are noninteracting, the quantum transport could be well solved by the density functional theory (DFT) in combination with the Landauer formula or the nonequilibrium Green's function [25,26]. However, if the Coulomb repulsions on those orbitals become strong enough, these approaches would fail, because the

correlation effects are treated at a mean-field-like level, and the excited spectrum cannot be captured properly [27]. Under such a circumstance, many-body nonperturbative methods are desired, within which the Wilson's numerical renormalization group (NRG) method is proved to be a reliable technique in dealing with the strongly correlated problems of quantum impurity models [25,26,28–32]. Hence, we adopt the NRG method to solve Eq. (1). The NRG method can provide us with much information about the static and thermodynamical properties on the entire energy scales. In our NRG calculation, we set the renormalization parameter Λ to be ∼2.5–3.0 and maintain around 3000 low-lying states at each iteration. Furthermore, a wide flat conduction electron density of states (DOS) $\rho_0 = 1/(2W_b)$ is used where W_b is the half bandwidth. The hybridization function between the conduction band and central monomers can then be written as $\Gamma = \pi\rho_0\tau^2$.

The spectral function of electron on the molecule at temperature T, $A_{ij}(\omega, T)$, is expressed as the imaginary part of the Green's function:

$$A_{ij}(\omega, T) = \sum_{\sigma} A_{ij\sigma}(\omega, T) = -\frac{1}{\pi}\sum_{\sigma} \mathrm{Im}G_{ij\sigma}(\omega, T). \quad (5)$$

Here, ω is the energy variable, and $G_{ij}(\omega)$ is the Fourier transformation of the retarded Green's function $G_{ij}(t)$ with

$$G_{ij\sigma}(t) = -i\theta(t)\langle\{d_{i\sigma}(t), d^{\dagger}_{j\sigma}\}\rangle. \quad (6)$$

If $i = j$, $A_{ii}(\omega, T)$ turns is the local density of states (LDOS) of electrons on the ith monomer orbital. In order to quantify the transport property, the linear conductance $G(T)$ through the QSCM at temperature T is obtained from the Landauer formula [33,34]:

$$G(T) = \frac{e^2}{h}\int\left[-\frac{\partial f(\omega)}{\partial\omega}\right]C(\omega, T)d\omega \quad (7)$$

with $f(\omega)$ denoting the Fermi-Dirac distribution function, and the transmission coefficient $C(\omega, T)$ is expressed as

$$C(\omega, T) = -\Gamma\sum_{i,j=1}^{2}\sum_{\sigma}\mathrm{Im}G_{ij\sigma}(\omega, T). \quad (8)$$

Throughout this paper, we set the Fermi level $\varepsilon_f = 0$. The zero temperature conductance $G(T = 0)$ in the limit of zero bias then can be defined as

$$G(T = 0) = \frac{e^2}{h}C(\omega = 0, T = 0). \quad (9)$$

To enhance the precision, we use a procedure of the full density matrix (FDM) to calculate the spectral density, which is done iteratively in the Anders-Schiller basis [35].

The temperature-dependent magnetic moment $\mu^2(T)$ and entropy $S_{\mathrm{mol}}(T)$ are given by the contribution of the molecule to the total magnetic moment and entropy of the whole system, respectively,

$$\mu^2(T) = \chi_{mol}k_BT/\left(g\mu_B^2\right) = \left\langle\mathbf{S}_z^2\right\rangle - \left\langle\mathbf{S}_z^2\right\rangle_0, \quad (10)$$

$$S_{mol}(T) = \frac{E - F}{T} - \frac{(E - F)_0}{T}. \quad (11)$$

Here, χ_{mol} is the contribution of the QSCM to the total magnetic susceptibility of the whole device at temperature T. k_B is the Boltzmann's constant, g is the electric gyromagnetic factor, and μ_B is the Bohr magneton. $\mathbf{S}_z$ is the total z component spin operator of the QSCM, and the subscript 0 refers to the situation when the QSCM is absent. Finally, $E = \langle H\rangle = \mathrm{Tr}[H\mathrm{e}^{-H/(k_BT)}]$ and $F = -k_BT\ln\mathrm{Tr}[e^{-H/(k_BT)}]$ are the total energy and free energy of the whole system, respectively.

III. RESULTS AND DISCUSSIONS

A. Itinerant electrons mediated ferromagnetic RKKY coupling between two side monomers and superexchange two-stage Kondo effect: Effect of Δ without t_1

First, we study the QPT and transport property of the QSCM affected by the energy difference between two central monomers Δ. We concentrate on the case that the two central monomers are not directly coupled with $t_1 = 0$. According to parameters in those real spin-crossover molecules [36,37], we set $U = 0.5$. The strongly correlated condition is illustrated by $U = 25\Gamma$. Furthermore, we fix $V_g = -U/2$, $t_2 = 0.001$ and $\epsilon_3 = \epsilon_4 = V_g$. ϵ_1 and ϵ_2 are defined as $\epsilon_1 = V_g + \Delta/2$ and $\epsilon_2 = V_g - \Delta/2$, respectively. Here, we have chosen the half bandwidth of the conduction lead W_b as the energy unit, which is about several eV in typical metal electrodes.

In Fig. 2(a) we show the numerical results of the electron occupation number on each monomer $\langle n_i\rangle$ at nearly zero temperature as a function of Δ. As Δ sweeps upwards, the occupation number of MM1 $\langle n_1\rangle$ decreases from 1.0 to 0.0 gradually due to an increasing energy level $\epsilon_1 = V_g + \Delta/2$, and $\langle n_2\rangle$ increases from 1.0 to 2.0 for its energy level while $\epsilon_2 = V_g - \Delta/2$ is reduced. In this process, the electron numbers for two side monomers MM3 and MM4 will always be 1.0, since ϵ_3 and ϵ_4 are fixed at the particle-hole (p-h) symmetric point.

The spin-spin correlation between different monomers $\langle\mathbf{S}_i\mathbf{S}_j\rangle$ are depicted in Fig. 2(b). It is seen that for small Δ, electrons on MM1 and MM2 are aligned parallelly because the strong U ($U \gg \Gamma, t_2$) favors each monomer to be singly occupied, and the effective Kondo couplings result in antiferromagnetic alignment of electrons on the central monomers and the electrodes. Therefore, a ferromagnetic RKKY interaction between electrons on two central monomers mediated by the Kondo couplings arises, mirroring $\langle\mathbf{S}_1\mathbf{S}_2\rangle \approx 1/4$. On the other side, electrons on MM1 (MM2) and MM3 (MM4) are organized antiparallelly with $\langle\mathbf{S}_1\mathbf{S}_3\rangle \approx -0.38$, because there exists an antiferromagnetic coupling induced by t_2. The above spin configuration then leads to a long-distance ferromagnetic superexchange coupling between two side monomers mediated by the spin triplet of two central monomers, reflected well by a parallel alignment with $\langle\mathbf{S}_3\mathbf{S}_4\rangle \approx 1/4$.

As Δ increases, $\langle\mathbf{S}_1\mathbf{S}_3\rangle$ changes from an antiferromagnetic correlation to an uncorrelated state around $\Delta \approx 0.5$, and the ferromagnetic configuration between two central monomers $\langle\mathbf{S}_1\mathbf{S}_2\rangle$ changes to an uncorrelated state too. These behaviors are caused by the fact that when Δ is relatively large such that $\Delta > U$, MM1 is in the empty state $|0\rangle$ and MM2 is

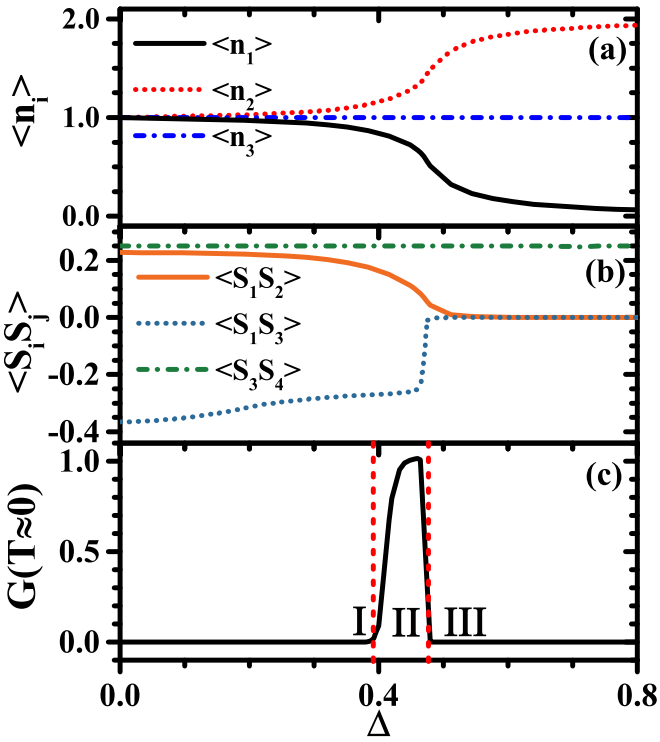

FIG. 2. (a) The electron occupation number on each monomer $\langle n_i\rangle$, (b) spin-spin correlation between different monomers i and j $\langle \mathbf{S}_i\mathbf{S}_j\rangle$, and (c) linear conductance $G(T\approx 0)$ at nearly zero temperature as a function of Δ. Here, $\langle n_4\rangle$ and $\langle \mathbf{S}_2\mathbf{S}_4\rangle$ are not shown due to $\langle n_3\rangle = \langle n_4\rangle$ and $\langle \mathbf{S}_2\mathbf{S}_4\rangle = \langle \mathbf{S}_1\mathbf{S}_3\rangle$. The other parameters are given by $\Gamma = 0.02$, $U = 0.5$, $V_g = -U/2$, $\epsilon_1 = V_g + \Delta/2$, $\epsilon_2 = V_g - \Delta/2$, $\epsilon_3 = \epsilon_4 = V_g$, $t_1 = 0$, and $t_2 = 0.001$.

in the fully occupied state $|\uparrow\downarrow\rangle$. We can also see that the value of $\langle \mathbf{S}_3\mathbf{S}_4\rangle$ remains a constant of about 1/4. Here, we stress that the underlying physical picture is distinguished from the small Δ case, due to the side monomers being nearly decoupled from their neighboring central ones. In fact, when MM1 is empty, while MM3 is singly occupied, there exists a superexchange coupling between electrons on MM3 and the electrodes. To obtain the strength of such a coupling, one may derive the effective Hamiltonian by using the perturbation theory in the tunneling matrix elements. The superexchange mechanism via the energy level ϵ_1 at MM1 can then be illustrated by the fourth order perturbation with respect to the tunneling matrix elements t_2 and τ. In the light of Ref. [38], we write the strength of the superexchange coupling J_{ISE} as follows:

$$J_{ISE} = 2\left(\frac{\sqrt{2}\tau t_2}{\epsilon_1}\right)^2\left[\frac{\epsilon_1^2 U - (\epsilon_3 - 2\epsilon_1)(\epsilon_1 - \epsilon_3)^2}{\epsilon_3(\epsilon_3 - 2\epsilon_1 - U)(\epsilon_1 - \epsilon_3)^2} + \frac{1}{\epsilon_3 + U}\right]. \tag{12}$$

For ϵ_1 and ϵ_3 given in our present model, the superexchange constant J_{ISE} further simplifies to

$$J_{ISE} = 16\left(\frac{\tau t_2}{\Delta - U}\right)^2\left[\frac{4U(\Delta - U)^2 - 2(U - 2\Delta)\Delta^2}{U\Delta^2(U + 2\Delta)} + \frac{2}{U}\right]. \tag{13}$$

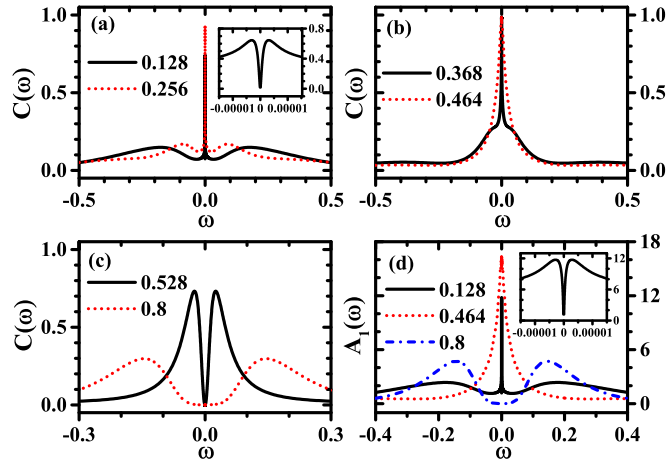

FIG. 3. (a)–(c) The transmission coefficient through the QSCM $C(\omega)$ at nearly zero temperature for various of Δ. (d) The local density of states (LDOS) of MM1 (MM2) $A_1(\omega)$ at nearly zero temperature for Δ in different regimes. Inset in (a) and (d): $C(\omega)$ and $A_1(\omega)$ for $\Delta = 0.128$ in an enlarged scale, which shows zero spectral weight at the Fermi level. The remaining parameters are given the same as in Fig. 2.

When $\langle n_1\rangle$ deviates from 1.0, J_{ISE} develops and it shows a divergence when $\Delta \to 0$ or U. Meanwhile, a similar superexchange coupling of the same quantity also exists between electrons on MM4 and the electrodes. Notice that J_{ISE} keeps positive, hence electrons on MM3 (MM4) and the electrodes are favored to be organized antiparallelly. As a result, electrons on MM3 and MM4 tend to be ferromagnetically aligned due to a long-distance RKKY interaction mediated by J_{ISE}. Since J_{ISE} also develops in the small nonzero Δ regime, the origination of the ferromagnetic configuration between MM3 and MM4 in this regime includes, in fact, both the superexchange coupling mediated by the spin triplet of two central monomers and the RKKY interaction mediated by J_{ISE}.

Figure 2(c) shows the linear conductance at nearly zero temperature $G(T\approx 0)$ as a function of Δ. One finds that the value of $G(T\approx 0)$ is always zero except a steep peak when Δ is moderate and in the range $\sim$[0.4, 0.47]. Thus, we can divide the physical process varied with Δ into three regimes. Regime I where the linear conductance is zero when Δ is small, regime II where $G(T\approx 0)$ has a peak where its maximum rises to nearly the unitary limit 1.0 when Δ is moderate, and regime III where the linear conductance drops abruptly to zero when Δ is large enough with $\Delta > \Delta_c \approx 0.47$. Detailed pictures could be found from the transmission coefficient through the QSCM $C(\omega)$ in Figs. 3(a)–3(c). It is seen that for Δ in regime I, e.g., $\Delta = 0.128$, $C(\omega)$ has two symmetric Coulomb peaks at about $\omega = \pm U/2$, but the spectral weight at the Fermi level is nearly zero [cf. inset in panel (a)], indicating zero conductance. Here, the suppression of the linear conductance is assisted by the Fano antiresonance: when t_2 is absent, the transport property of such a device is dominant by the underscreened spin-1 Kondo effect, resulting in a full conductance [39,40]. However, once t_2 turns on, the Kondo peak at the Fermi level splits, and a dip at $\omega = 0$ develops, which is the so-called Fano antiresonance dip. This behavior could be attributed to a destructive interference of the quantum amplitudes for the

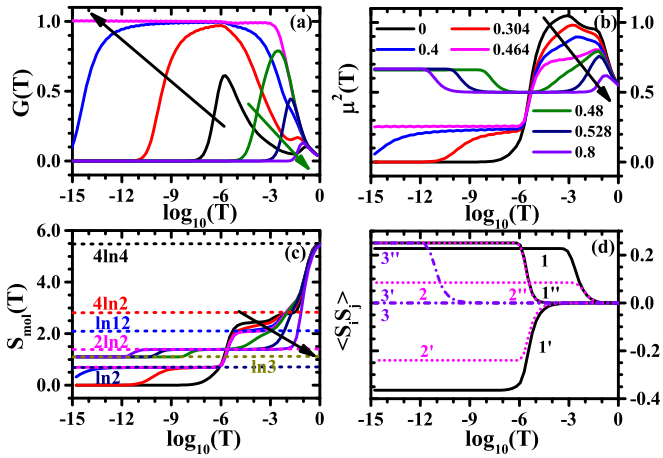

FIG. 4. Temperature-dependent (a) $G(T)$, (b) local magnetic moment $\mu^2(T)$, and (c) entropy $S_{mol}(T)$ for the QSCM as functions of temperature T in terms of different Δ. Curves in (a) along the black arrow are for $\Delta = 0$, 0.304, 0.4, and 0.464, and curves along the olive arrow are for $\Delta = 0.48$, 0.528, and 0.8, respectively. (d) $\langle \mathbf{S}_i\mathbf{S}_j\rangle$ between MMs i and j versus $\log_{10}(T)$ for $\Delta = 0$, 0.464, and 0.8, respectively. Curves 1–3 in panel (d) are for $\langle \mathbf{S}_1\mathbf{S}_2\rangle$, $1'$–$3'$ are for $\langle \mathbf{S}_1\mathbf{S}_3\rangle$, and $1''$–$3''$ are for $\langle \mathbf{S}_3\mathbf{S}_4\rangle$. Curves for each Δ in the four panels are unified with the same color. The remaining parameters are the same as in Fig. 2 unless otherwise specified.

conduction pathway directly through the central monomers without passing through the side monomers and the indirect conduction pathway through the side monomers via t_2 [41].

When Δ gradually increases, the position of the Coulomb peaks and the shoulders of the central dip move close to the Fermi level. And finally, they fuse into one peak as the system moves into regime II, which can be clearly seen from Fig. 3(b). The peak at the Fermi level suggests that the tunneling process happens, and the value of $G(T \approx 0)$ reaches 1.0. This behavior can be attributed to the fact that when Δ increases close to U, J_{ISE} is enhanced. Thus, the superexchange-induced Kondo effect develops, which corresponds to the process of the local magnetic moments on the side monomers that partially screened by the itinerant electrons tunneling virtually through the central monomers [38], as will be discussed in detail in the following. As Δ increases further to regime III, the peak splits again. In this regime, J_{ISE} becomes extremely small, hence impedes the superexchange-induced Kondo effect to happen. An increasing Δ will decrease the height of the peak and push the symmetrical peak positions far away from the Fermi level, for the energy level, ϵ_1 (ϵ_2) is lifted up (descended down), cf., Fig. 3(c). The above Kondo effect could also be clarified by the LDOS of the central monomers $A_1(\omega)$ as is shown in Fig. 3(d). For both small and large enough Δ, the spectral weights at the Fermi level of $A_1(\omega)$ are nearly zero, while for moderate Δ, an obvious peak develops, inferring the Kondo behavior.

Now we focus on the thermodynamic properties of the system. In Fig. 4, we show the temperature-dependent linear conductance $G(T)$, local magnetic moment $\mu^2(T)$, and entropy $S_{mol}(T)$ of the QSCM, as well as the spin correlation $\langle \mathbf{S}_i\mathbf{S}_j\rangle$ between monomers i and j. The thermodynamic properties show distinct behaviors in different temperature scales. When $T/U > 1$, we notice that $G(T) \approx 0$ for all Δ. Because in this high temperature scale, the local electrons on each monomer are independent with $\langle \mathbf{S}_i\mathbf{S}_j\rangle = 0$, and the possible states $|0\rangle$, $|\uparrow\rangle$, $|\downarrow\rangle$, $|\uparrow\downarrow\rangle$ in each monomer are equally probable. Hence, each monomer contributes 1/8 to $\mu^2(T)$ and $\ln 4$ to $S_{mol}(T)$, resulting in total quantities $\mu^2(T) \approx 1/2$, $S_{mol}(T) \approx 4\ln 4$. As T decreases to the regime $\Gamma < T \leqslant U$, U begins to come into play. The influence of U makes each monomer singly occupied, and thus the states $|0\rangle$ and $|\uparrow\downarrow\rangle$ are inhibited. Each monomer then contributes 1/4 to $\mu^2(T)$ and $\ln 2$ to $S_{mol}(T)$, leading to $\mu^2(T) \approx 1.0$ and $S_{mol}(T) \approx 4\ln 2$. Transport in this regime is mainly dominated by the cotunneling process, which results in a narrow plateau in the appearance of $G(T)$ [42,43].

When $T \leqslant \Gamma$, the properties for $\Delta < \Delta_c$ and $\Delta \geqslant \Delta_c$ are quite different. For $\Delta < \Delta_c$, e.g., $\Delta = 0.0$, the formation of a local triplet state between two central monomers develops due to the ferromagnetic RKKY interaction J_{RKKY}, thus one observes a maximum value of $\mu^2(T)$. This tendency is confirmed by the fact that $\langle \mathbf{S}_1\mathbf{S}_2\rangle$ grows from zero to about 1/4, cf., panel 4(d). In this case, the two central monomers contribute $S_{CMM}(S_{CMM}+1)/3 = 2/3$ to $\mu^2(T)$ and $\ln(2S_{CMM}+1) = \ln 3$ to $S_{mol}(T)$, leading to total quantities $\mu^2(T) \approx 2/3 + 1/4 \times 2 = 7/6$ and $S_{mol}(T) \approx \ln 3 + 2\ln 2 = \ln 12$. Correspondingly, the value of $G(T)$ increases gradually until a maximum value of about 0.6 due to the level broadening of the local orbital in the central monomers. When $T \ll J_2 = 4t_2^2/U$, the linear conductance plateau goes back to zero. Because in this regime the electron in MM1 (MM2) forms a spin singlet with that in MM3 (MM4), reflected by $\langle \mathbf{S}_1\mathbf{S}_3\rangle$, it decreases to about -0.38, and the destructive quantum interference suppresses the linear conductance. Meanwhile, $\mu^2(T)$ and $S_{mol}(T)$ drop to zero, while $\langle \mathbf{S}_3\mathbf{S}_4\rangle$ grows to nearly 1/4.

For larger Δ, the high conductance window is enlarged. Specifically, $G(T)$ increases to its unitary limit of 1.0 at a higher temperature, while it weakens to zero at a lower temperature. Therefore, for a fixed low temperature, $G(T \to 0)$ increases continuously, revealing an image of Fig. 2(c). This behavior is attributed to the following fact. When Δ sweeps upwards, the RKKY interaction between two central monomers J_{RKKY} decreases, for J_{RKKY} favors two central monomers to be singly occupied. The related plateau in $\mu^2(T)$ then reduces to mix with that caused by U, see the black line to the purple line along the black arrow in Fig. 4(b). The relevant energy scale is dominated by U, hence $G(T)$ grows to 1.0 early from the cotunneling process. In this process, $\mu^2(T)$ is screened in two stages, e.g., $\Delta = 0.304$ in panel (b). In the first stage, the magnetic moments of the side monomers are partially screened by the central monomers at a temperature $T_{K1} \sim 10^{-5}$ due to t_2, giving platforms of 1/4 to $\mu^2(T)$ and ln2 to $S_{mol}(T)$. Then that of the remaining is screened by the electrodes at a lower temperature T_{K2} due to the superexchange interaction J_{ISE}. It is seen that T_{K2} decreases with Δ ($\Delta < U$), and could be fitted by the following formula:

$$T_{K2} = c_1 T_{K1} \exp(-c_2 T_{K1}/J_{ISE}). \tag{14}$$

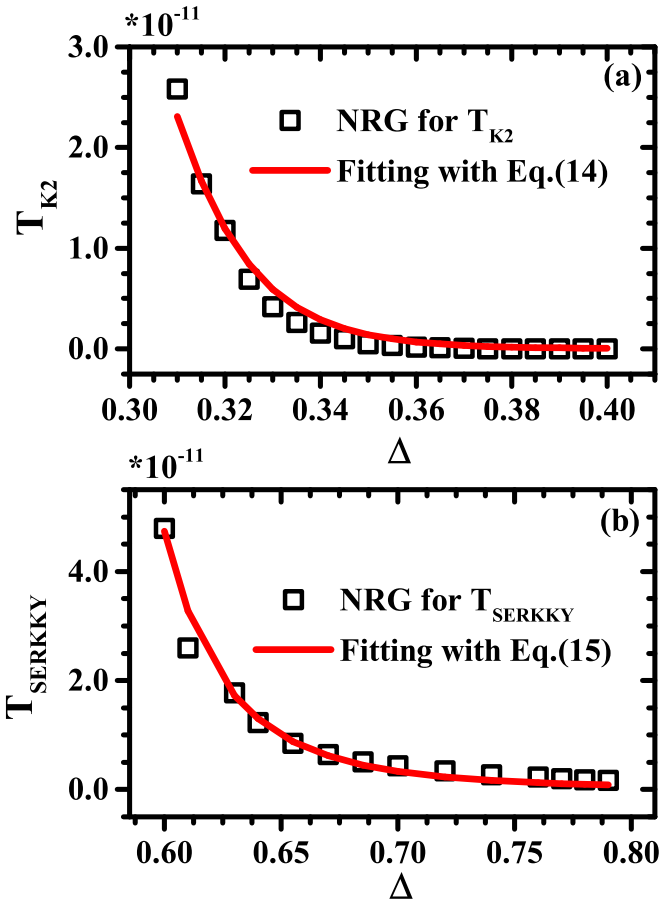

FIG. 5. (a) T_{K2} and (b) T_{SERKKY} as functions of Δ. Scatter plots are captured from our NRG data, while the solid curves are the fitting functions. The other parameters are the same as in Fig. 2.

Here, T_{K2} is defined by the temperature corresponding to the half maximum of $\mu^2(T)$ where $\mu^2(T)$ decreases from the platform of $1/4$ to zero. In Fig. 5(a), we show the results fitted by Eq. (14). One may see that it has a good agreement with the numerical results, where the fitting parameters are given by $c_1 = 7.3 * 10^{-11}$ and $c_2 = -5.7$. This behavior shows a clear crossover from the zero conductance regime to the high conductance regime around the temperature indicated by T_{K2}, thus the enlargement of the high conductance window is achieved. These results imply that the above phenomenon occurring in $G(T)$ and $\mu^2(T)$ is in essence a two-stage Kondo effect [43–47]. However, singular manifestations are identified. As is known, in typical side-coupled double quantum dot systems, the fitting parameters c_1 and c_2 are some constants of the order 1.0 [43,44,46], whereas in our present model, c_1 becomes extremely small. Because the magnetic moments of the side monomers are screened by the superexchange coupling, rather than the direct interaction, where the latter one is always far more large than the former one. Furthermore, in our present system, c_2 is negative, differing from the case of positive value in the typical two-stage Kondo effect. This is resulted from the fact that T_{K2} in our model decreases with increasing Δ, while in the typical two-stage Kondo effect, T_{K2} varies in a contrary tendency as the interdot hopping increases [43,44,46].

When Δ is large enough in regime III, e.g., $\Delta = 0.48$, the images of $\mu^2(T)$ and $S_{mol}(T)$ show a significant change. With increasing Δ, the cotunnelling process is suppressed gradually. Note that in this case, $G(T)$ weakening to zero can occur in higher temperatures, indicating that the temperature window for the cotunnelling process to occur is becoming narrower, see the trend of the green arrows in Fig. 4(a). In this case, $\mu^2(T)$ and $S_{mol}(T)$ decrease to a platform with $\mu^2(T) = 1/2$ and $S_{mol}(T) = 2\ln 2$ at a scale $T \sim U$, respectively, for electrons in the two side monomers are in the local moment regime. When T becomes lower, e.g., $T \sim 10^{-9}$, $\mu^2(T)$ increases to a higher value of about 0.67, which is resulted from the RKKY interaction between two side monomers mediated by J_{ISE}, and a spin triplet is generated with an effective spin $S_{SMM} = 1$. Meanwhile, $S_{mol}(T)$ decreases to about ln3, satisfying that $S_{mol}(T) = \ln(2S_{SMM} + 1)$. This behavior is well confirmed by the process where $\langle \mathbf{S}_3\mathbf{S}_4 \rangle$ increases to $1/4$, cf., Fig. 4(d). The temperature T_{SERKKY}, where the high magnetic moment platform develops, decreases with increasing Δ as per relation

$$T_{\text{SERKKY}} = c_3 J_{\text{SERKKY}}, \tag{15}$$

with the fitting parameter given by $c_3 = 0.00028$, and J_{SERKKY} the superexchange coupling mediated RKKY interaction between two side monomers, which we evaluate as [48]

$$J_{\text{SERKKY}} = U(\rho_0 J_{ISE})^2. \tag{16}$$

In Fig. 5(b), we show the results fitted by Eq. (15). One notices they are consistent with our NRG results. These conclusions are similar to those between the RKKY interaction J_{RKKY} and the RKKY temperature T_{RKKY} in the parallel multi-quantum-dot systems [48], but with a more small fitting parameter, due to a more complex geometry.

B. Spin singlet mediated antiferromagnetic coupling between two side monomers: Effect of t_1 with $\Delta = 0$

Then we turn to the case when the hopping integral between two central monomers t_1 is applied. We first concentrate on the case that the energy levels for four monomers are identical with $\epsilon_i = -U/2$. In Fig. 6(a) we show the numerical results of $\langle \mathbf{S}_i\mathbf{S}_j \rangle$ as functions of t_1. It is seen that when t_1 exceeds a critical point $t_{1c} \approx 0.019$, $\langle \mathbf{S}_1\mathbf{S}_2 \rangle$ drops to about -0.7, due to the antiferromagnetic coupling induced by t_1 overwhelming the ferromagnetic RKKY interaction between electrons on two central monomers. In this process, $\langle \mathbf{S}_3\mathbf{S}_4 \rangle$ also jumps to a negative value of about $-3/4$, indicating an ideal spin singlet of two side monomers. However, one can hardly attribute this spin configuration to the antiferromagnetic coupling between the central monomers and their neighboring side units, because they are nearly decoupled from each other with $\langle \mathbf{S}_1\mathbf{S}_3 \rangle \approx 0$. To explore the origin of the antiferromagnetic coupling between two side monomers, we make a Schrieffer-Wolff transformation [49] to the isolated QSCM system, which maps the present four impurity Anderson model to a four impurity spin-1/2 Kondo model. The effective Hamiltonian of Eq. (3) then can be written as

$$H_{\text{eff}} = J_1\mathbf{S}_1 \cdot \mathbf{S}_2 + J_2\mathbf{S}_1 \cdot \mathbf{S}_3 + J_2\mathbf{S}_2 \cdot \mathbf{S}_4, \tag{17}$$

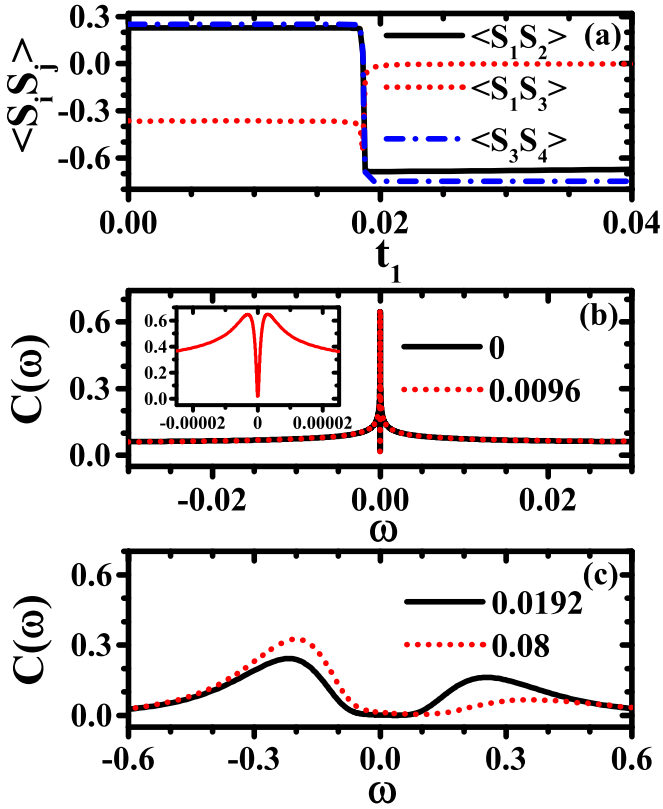

FIG. 6. (a) $\langle \mathbf{S}_i \mathbf{S}_j \rangle$ at nearly zero temperature as functions of t_1. (b), (c) $C(\omega)$ at nearly zero temperature for various t_1. Inset in (b): $C(\omega)$ for $t_1 = 0.0096$ in an enlarged scale. The other parameters are given by $\Gamma = 0.02$, $U = 0.5$, $\Delta = 0$, $V_g = -U/2$, $\epsilon_1 = V_g + \Delta/2$, $\epsilon_2 = V_g - \Delta/2$, $\epsilon_3 = \epsilon_4 = V_g$, and $t_2 = 0.001$.

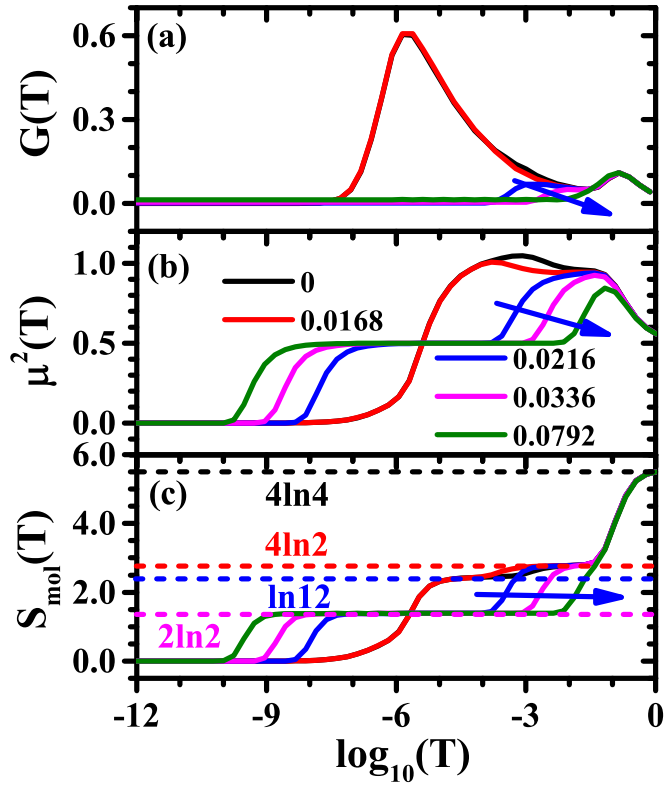

FIG. 7. Temperature-dependent (a) $G(T)$, (b) $\mu^2(T)$, and (c) $S_{mol}(T)$ for the QSCM device in terms of different t_1. Curves in panels (a)–(c) are for $t_1 = 0$, 0.0168, 0.0216, 0.0336, and 0.0792, respectively. The remaining parameters are the same as in Fig. 6.

with $J_1 = 4t_1^2/U$, $J_2 = 4t_2^2/U$, and $\mathbf{S}_i$ the spin operator of MMi. When $J_2 \ll J_1$, i.e., $t_2 \ll t_1$, a superexchange coupling between two side spins $\mathbf{S}_3$ and $\mathbf{S}_4$ then occurs when two central spins $\mathbf{S}_1$ and $\mathbf{S}_2$ are configured as a singlet via virtual excitation to the triplet configurations [5]. Dropping a constant and going to the third order of J_2, the effective superexchange Hamiltonian between spins $\mathbf{S}_3$ and $\mathbf{S}_4$ takes the Heisenberg exchange form

$$H_{SSE} = J_{SSE} \mathbf{S}_3 \cdot \mathbf{S}_4, \tag{18}$$

where J_{SSE} denotes the singlet mediated long-distance superexchange coupling, which can be written as [5,23]

$$J_{SSE} = \frac{2J_2^2}{J_1}\left(1 + \frac{3J_2}{2J_1}\right). \tag{19}$$

Therefore, when $t_1 > t_{1c}$, to reduce the total energy of the system, the spins on two side monomers favor to be antiferromagnetically organized. The discontinuous change of $\langle \mathbf{S}_i \mathbf{S}_j \rangle$ indicates the transition at t_{1c} is a first order QPT. The critical point t_{1c} satisfies that the ferromagnetic RKKY interaction J_{RKKY} equals to the direct antiferromagnetic exchange interaction J_1 between two central monomers, viz., $0.62 * 64\Gamma^2/(\pi^2 U) = 4t_{1c}^2/U$ [48,50], giving $t_{1c} \approx \Gamma$.

Figures 6(b) and 6(c) present the transmission coefficient at nearly zero temperature $C(\omega)$ for different t_1. It is seen that for both $t_1 < t_{1c}$ and $t_1 \geqslant t_{1c}$, the spectral weights of $C(\omega)$ at the Fermi level $\omega = 0$ are nearly zero, illustrating zero conductance for both cases. For $t_1 < t_{1c}$, e.g., $t_1 = 0.0096$, the suppression of the linear conductance is assisted by the destructive interference as is mentioned above. For $t_1 \geqslant t_{1c}$, e.g., $t_1 = 0.0192$, the spin singlet between two central monomers decouples the QSCM from the electrodes, hence electrons can not transfer from the left to the right electrodes, suggesting zero conductance.

In Fig. 7, we show the temperature-dependent $G(T)$, $\mu^2(T)$, and $S_{mol}(T)$. For small t_1, the tendencies of these physical quantities are similar to the case of $t_1 = 0$. When t_1 is large, e.g., curves along the blue arrow in Fig. 7, the plateaus of $\mu^2(T)$ and $S_{mol}(T)$ disappear in the regime of $T \sim J_{RKKY}$. Instead, they weaken to plateaus of 0.5 and 2ln2, respectively. Because the direct antiferromagnetic coupling between two central monomers J_1 destroys the influence of J_{RKKY}, then $\mu^2(T)$ and $S_{mol}(T)$ are only contributed by the side monomers, which are still in the local moment regime in this temperature scale. The temperature where $\mu^2(T)$ and $S_{mol}(T)$ drop to this regime grows gradually with increasing t_1, since J_1 becomes larger.

When T sweeps downwards to a smaller value, e.g., $T \approx 10^{-7} \sim 10^{-8}$ for $t_1 = 0.0216$, both $\mu^2(T)$ and $S_{mol}(T)$ decrease to zero for the spin singlet between MM3 and MM4 generates. The related temperature T_{SSE}, where $\mu^2(T)$ and $S_{mol}(T)$ drop to zero, decreases gradually with increasing t_1, since J_{SSE} monotonically decreases with increasing t_1. This behavior confirms again our conclusion illustrated by

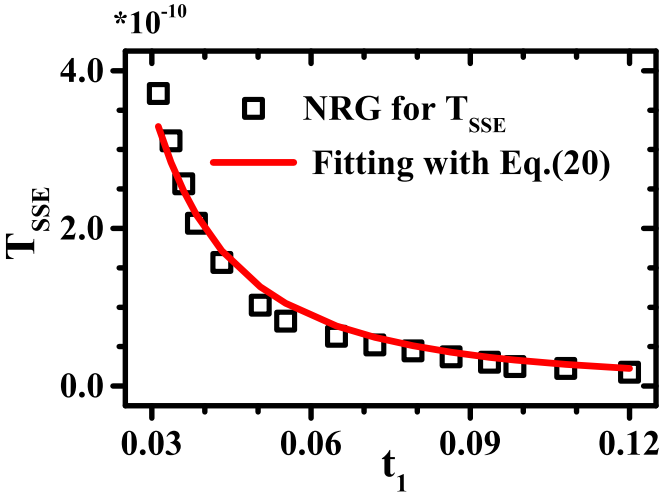

FIG. 8. The temperature scale T_{SSE}, which refers to the spin singlet mediated long-distance antiferromagnetic exchange coupling between two side monomers J_{SSE}, as a function of t_1. Scatter plots are captured from our NRG data, and the solid curve is the fitting function. The other parameters are the same as in Fig. 6.

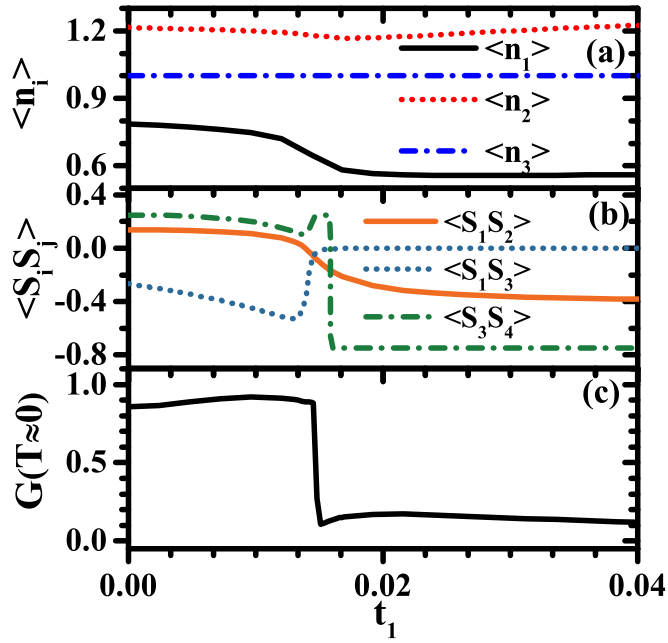

FIG. 9. (a) $\langle n_i\rangle$, (b) $\langle \mathbf{S}_i\mathbf{S}_j\rangle$, and (c) $G(T\approx 0)$ at nearly zero temperature as functions of t_1 with fixed $\Delta = 0.428$. The other parameters are given the same as Fig. 6 unless otherwise specified.

Eq. (19). $G(T)\approx 0$ in nearly all temperature scales for the resonant process is also suppressed by $t_1 > \Gamma$.

To make a deep understanding of the above temperature scale, we depict T_{SSE} and its fitting function versus t_1 in Fig. 8. Here, T_{SSE} is captured from our NRG data and is defined by the temperature corresponding to the half maximum of $\mu^2(T)$ where $\mu^2(T)$ decreases from 0.5 to 0.0. One may see T_{SSE} decreases as t_1 sweeps upwards, and could be illustrated by a function of J_{SSE}:

$$T_{SSE} = c_4 J_{SSE}, \tag{20}$$

where the fitting parameter is given by $c_4 = 0.2$. One finds the fitting function is consistent with our NRG results.

C. Competition between the itinerant electrons and the spin singlet mediated long-distance couplings

We then discuss the effect of t_1 when Δ is fixed in regime II, e.g., $\Delta = 0.428$. It is seen that if t_1 is small, the quantum phase is similar to the case of $t_1 = 0$, see Figs. 9(a)–9(c). However, before the spin singlet between two side monomers develops for large t_1, the system experiences a singular quantum phase around $t_1 = 0.013$, distinguishing from the case in Sec. III B. In such a phase, MM1 and MM2 are antiparallelly organized due to t_1. Meanwhile, the side monomers decouple from their neighboring central monomers with $\langle \mathbf{S}_1\mathbf{S}_3\rangle = 0$, while two side monomers hold in a ferromagnetic alignment but with an enhanced value where $\langle \mathbf{S}_3\mathbf{S}_4\rangle$ increases to a plateau. In this regime, the superexchange spin-1 Kondo effect is dominant, hence $G(T\approx 0)$ holds at a high level, see Fig. 9(c). This QPT is resulted from the competition between the ferromagnetic RKKY interaction J_{RKKY} and the direct antiferromagnetic exchange interaction J_1 of two central monomers, giving a critical point $t_{1,c1}$, which satisfies $J_{RKKY}\approx J_1$. Here, $t_{1,c1}$ is significantly smaller than Γ, since $\langle n_1\rangle$ and $\langle n_3\rangle$ deviate from the p-h symmetric case of 1.0 [cf. Fig. 9(a)], which then leads to a smaller J_{RKKY} [48].

If t_1 grows to another critical point $t_{1,c2}\approx 0.016$, the antiferromagnetic correlation of MM1 and MM2 is enhanced with $\langle \mathbf{S}_1\mathbf{S}_2\rangle \approx -0.4$, and $\langle \mathbf{S}_3\mathbf{S}_4\rangle$ decreases from 0.18 to -0.75, indicating the center monomers decouple from their corresponding side monomers and the long-distance superexchange between two side monomers develops. The QSCM seems like a quasiisolated system, hence $G(T\approx 0)$ becomes small. This QPT is attributed to the competition between the itinerant electrons mediated ferromagnetic RKKY coupling and the spin singlet mediated antiferromagnetic coupling of two side monomers, satisfying $J_{SERKKY}\approx J_{SSE}$.

The thermodynamic properties of the system clearly reflect the above competitions. In Fig. 10, we display the temperature-dependent $G(T)$, $\mu^2(T)$, $S_{mol}(T)$, and $\langle \mathbf{S}_i\mathbf{S}_j\rangle$. For small t_1, the tendencies of these physical quantities are similar to the case of Δ located in regime II in Fig. 2(c). When t_1 exceeds $t_{1,c1}$, e.g., the blue line for $t_1 = 0.0145$ in Fig. 10, $\mu^2(T)$ and $S_{mol}(T)$ decrease from the local moment regime to platforms of $\mu^2(T) = 0.5$ and $S_{mol}(T) = 2\ln 2$, respectively, if T sweeps downwards to about $T\sim 10^{-5}$. Because an antiferromagnetic configuration between two central monomers develops, mirroring $\langle \mathbf{S}_1\mathbf{S}_2\rangle$ weakens to a negative value, cf., Fig. 10(d). In this case, the side monomers are decoupled from the central ones, and each of them contributes 1/4 and ln2 to $\mu^2(T)$ and $S_{mol}(T)$, respectively. When T reaches to about $T\sim 10^{-8}$, $\mu^2(T)$ rises to a higher platform, because $\mu^2(T) = S_{SMM}(S_{SMM}+1)/3 = 2/3$ caused by a spin triplet of two side monomers is generated, giving an effective spin $S_{SMM} = 1$. In this case, $S_{mol}(T) = \ln(2S_{SMM}+1) = \ln 3$ develops. This behavior is also reflected by the fact that $\langle \mathbf{S}_3\mathbf{S}_4\rangle$ increases to about 1/4. In these two temperature regimes, $G(T)$ holds at a low level, due to the spin singlet of two central monomers. However, if T is low enough, $\mu^2(T)$ and $S_{mol}(T)$ decrease to 1/4 and ln2, respectively, due to the superexchange Kondo

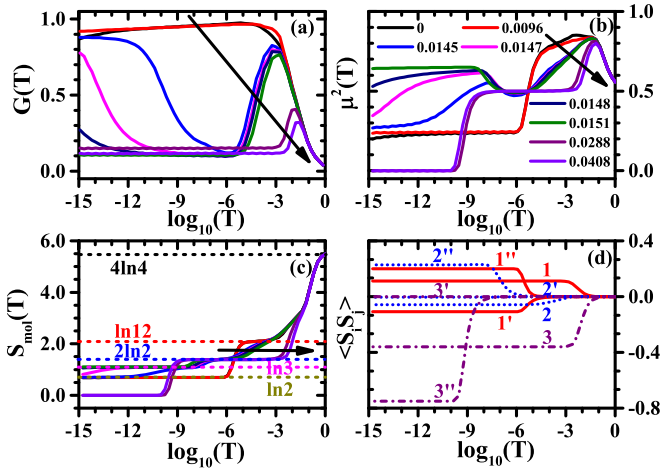

FIG. 10. Temperature-dependent (a) $G(T)$, (b) $\mu^2(T)$, and (c) $S_{mol}(T)$ of the QSCM device as functions of $\log_{10}(T)$ in terms of different t_1. Curves in these panels are for $t_1 = 0$, 0.0096, 0.0145, 0.0147, 0.0151, 0.0288, and 0.0408, respectively. (d) $\langle \mathbf{S}_i\mathbf{S}_j\rangle$ between MMi and MMj versus $\log_{10}(T)$ for $t_1 = 0.0096$, 0.0145, and 0.0288. Curves 1–3 are for $\langle \mathbf{S}_1\mathbf{S}_2\rangle$, 1′–3′ are for $\langle \mathbf{S}_1\mathbf{S}_3\rangle$, and 1″–3″ are for $\langle \mathbf{S}_3\mathbf{S}_4\rangle$. Curves for each t_1 in these four panels are unified with the same color. The remaining parameters are the same as in Fig. 9.

effect occurring and one of the side spins being screened by electrons on the electrodes. As a result, $G(T)$ rises to a higher level. When $t_1 > t_{1,c2}$, the situation is similar to the case of previous lager t_1 in Sec. III B.

IV. CONCLUSION

To conclude, we have studied the QPTs and electronic transport properties of a QSCM device at zero and finite temperatures assisted by various kinds of superexchange couplings in the strongly correlated limit. In the QSCM, two monomers are embedded in two metal electrodes, and the other two monomers are side coupled to their neighboring central monomers. When the hopping between two central monomers t_1 is absent, adjusting the energy level spacing Δ then induces the zero-temperature linear conductance $G(T \approx 0)$ to reach its unitary limit when Δ is in the intermediate regime. In such a regime, there exists a superexchange coupling between electrons on MM3 (MM4) and the electrodes. This kind of superexchange coupling then mediates a long-distance ferromagnetic RKKY interaction between two side monomers. Both of the above superexchange couplings can be manifested by the magnetic moment and entropy at abundant low temperature. Furthermore, a superexchange two-stage Kondo effect is also clarified, which is well illustrated by the evolutions of the local magnetic moment and spectral properties.

When t_1 is applied where Δ is absent, one finds another kind of long-distance superexchange coupling between two side monomers mediated by the spin singlet of two central monomers when $t_1 \gg t_2$. This coupling results in an antiferromagnetic configuration between two side monomers. The spin configuration of the four units then isolates the device from the electrodes, hence zero conductance could be found. Temperature-dependent images and numerical simulations confirm well the above conclusions. If Δ is fixed at an intermediate value, applying t_1 then triggers a singular quantum phase, where two central monomers are antiparallelly organized, whereas two side ones are aligned ferromagnetically. Superexchange Kondo effect appears at low-enough temperature.

To be realized experimentally, we recommend the isomers of the nickel tetraphenylporphyrin (Ni-TPP) molecule as the best candidate of the QSCM. Such a molecule is predicted to be an ideal framework for exploring the hybridization-induced spin crossover, and a minimal quadruple orbital model that captures the essence of the spin-state switching is proposed, which is found to provide good insight into the underlying physics [36]. Furthermore, a Fe-porphyrin (FeP) molecule could also be an alternative candidate. Based on this molecule, a mechanical spin-switch device is designed, in which external strain triggers the intrinsic magnetostructural coupling through a purely organic embedding, and a low-spin ($S = 1$) to high-spin ($S = 2$) crossover is demonstrated by tensile strain [37]. More broadly, depending on the specific geometry and the strength of the ligand field, spin-crossover molecules may switch between a low-spin and a high-spin state as a function of temperature, illumination, pressure, and magnetic or electric field [51–62]. During the last years, spin-crossover molecules have attracted much research interest, for it offers unique opportunities for the discovery of fundamental physical phenomena that are not accessible in bulk materials studied with traditional approaches, as well as that it is desirable for molecule-based switching and memory applications [51,52,63–67].

We believe that the above findings not only clarify the relevant physical pictures of the QPTs and the transport properties induced by different long-distance superexchange interactions in a quadripartite spin chain, but they may also provide important guidelines for tailoring molecular devices or nanoscale semiconductor tunneling devices on demands.

ACKNOWLEDGMENTS

This work is financially supported by the Natural Science Foundation of Hubei Province under Grants No. 2023AFB456 and No. 2023AFB891, the open fund of Hubei Key Laboratory of Energy Storage and Power Battery (HUAT) under Grant No. ZDK22023A04, the Chunhui Program of Ministry of Education under Grant No. HZKY20220337, and the Science and Technology Innovation Team Research Fund (Institute of Shiyan Industrial Technology of Chinese Academy of Engineering) under Grant No. ZCTD202201.

[1] A. C. Hewson, *The Kondo Problem to Heavy Fermions* (Cambridge University Press, Cambridge, England, 1997).

[2] P. Coleman, *Introduction to Many-Body Physics* (Cambridge University Press, Cambridge, England, 2015).

[3] T. A. Baart, T. Fujita, C. Reichl, W. Wegscheider, and L. M. K. Vandersypen, Coherent spin-exchange via a quantum mediator, Nat. Nanotechnol. **12**, 26 (2017).

[4] F. K. Malinowski, F. Martins, T. B. Smith, S. D. Bartlett, A. C. Doherty, P. D. Nissen, S. Fallahi, G. C. Gardner, M. J. Manfra, C. M. Marcus, and F. Kuemmeth, Fast spin exchange across a multielectron mediator, Nat. Commun. **10**, 1196 (2019).

[5] H. Qiao, Y. P. Kandel, S. Fallahi, G. C. Gardner, M. J. Manfra, X. Hu, and J. M. Nichol, Long-distance superexchange between semiconductor quantum-dot electron spins, Phys. Rev. Lett. **126**, 017701 (2021).

[6] N. J. Craig, Tunable nonlocal spin control in a coupled-quantum dot system, Science **304**, 565 (2004).

[7] R. M. Potok, I. G. Rau, H. Shtrikman, Y. Oreg, and D. Goldhaber-Gordon, A tunable Kondo effect in quantum dots, Nature (London) **446**, 167 (2007).

[8] J. C. Oberg, M. R. Calvo, F. Delgado, M. Moro-Lagares, D. Serrate, D. Jacob, J. Fernández-Rossier, and C. F. Hirjibehedin, Control of single-spin magnetic anisotropy by exchange coupling, Nat. Nanotechnol. **9**, 64 (2014).

[9] J. Medford, J. Beil, J. M. Taylor, S. D. Bartlett, A. C. Doherty, E. I. Rashba, D. P. DiVincenzo, H. Lu, A. C. Gossard, and C. M. Marcus, Self-consistent measurement and state tomography of an exchange-only spin qubit, Nat. Nanotechnol. **8**, 654 (2013).

[10] H. Flentje, P.-A. Mortemousque, R. Thalineau, A. Ludwig, A. D. Wieck, C. Buerle, and T. Meunier, Coherent long-distance displacement of individual electron spins, Nat. Commun. **8**, 501 (2017).

[11] T. Nakajima, A. Noiri, J. Yoneda, M. R. Delbecq, P. Stano, T. Otsuka, K. Takeda, S. Amaha, G. Allison, K. Kawasaki, A. Ludwig, A. D. Wieck, D. Loss, and S. Tarucha, Quantum non-demolition measurement of an electron spin qubit, Nat. Nanotechnol. **14**, 555 (2019).

[12] B. Jadot, P. Mortemousque, E. Chanrion, V. Thiney, A. Ludwig, A. D. Wieck, M. Urdampilleta, C. Bäuerle, and T. Meunier, Distant spin entanglement via fast and coherent electron shuttling, Nat. Nanotechnol. **16**, 570 (2021).

[13] A. Noiri, K. Takeda, T. Nakajima, T. Kobayashi, A. Sammak, G. Scappucci, and S. Tarucha, A shuttling-based two-qubit logic gate for linking distant silicon quantum processors, Nat. Commun. **13**, 5740 (2022).

[14] K. W. Chan, H. Sahasrabudhe, W. Huang, Y. Wang, H. C. Yang, M. Veldhorst, J. C. C. Hwang, F. A. Mohiyaddin, F. E. Hudson, K. M. Itoh, A. Saraiva, A. Morello, A. Laucht, R. Rahman, and A. S. Dzurak, Exchange coupling in a linear chain of three quantum-dot spin qubits in silicon, Nano Lett. **21**, 1517 (2021).

[15] G. X. Chan, P. Huang, and X. Wang, Universal control of superexchange in linear triple quantum dots with an empty mediator, Phys. Rev. B **108**, 035402 (2023).

[16] V. Srinivasa, H. Xu, and J. M. Taylor, Tunable spin-qubit coupling mediated by a multielectron quantum dot, Phys. Rev. Lett. **114**, 226803 (2015).

[17] R. Sánchez, F. Gallego-Marcos, and G. Platero, Superexchange blockade in triple quantum dots, Phys. Rev. B **89**, 161402(R) (2014).

[18] L. Campos Venuti, C. D. E. Boschi, and M. Roncaglia, Long-distance entanglement in spin systems, Phys. Rev. Lett. **96**, 247206 (2006).

[19] P. Stano, D. Loss, Review of performance metrics of spin qubits in gated semiconducting nanostructures, Nat. Rev. Phys. **4**, 672 (2022).

[20] S. Oh, L. A. Wu, Y. P. Shim, J. Fei, M. Friesen, and X. Hu, Heisenberg spin bus as a robust transmission line for quantum-state transfer, Phys. Rev. A **84**, 022330 (2011).

[21] Y. P. Kandel, H. Qiao, S. Fallahi, G. C. Gardner, M. J. Manfra, and J. M. Nichol, Adiabatic quantum state transfer in a semiconductor quantum-dot spin chain, Nat. Commun. **12**, 2156 (2021).

[22] A. Wójcik, T. Łuczak, P. Kurzyński, A. Grudka, T. Gdala, and M. Bednarska, Unmodulated spin chains as universal quantum wires, Phys. Rev. A **72**, 034303 (2005).

[23] Y. P. Kandel, H. Qiao, and J. M. Nichol, Perspective on exchange-coupled quantum-dot spin chains, Appl. Phys. Lett. **119**, 030501 (2021).

[24] N. A. Zimbovskaya, and M. R. Pederson, Electron transport through molecular junctions, Phys. Rep. **509**, 1 (2011).

[25] M. Thoss, and F. Evers, Theory of quantum transport in molecular junctions, J. Chem. Phys. **148**, 030901 (2018).

[26] F. Evers, R. Korytár, S. Tewari, and J. M. van Ruitenbeek, Advances and challenges in single-molecule electron transport, Rev. Mod. Phys. **92**, 035001 (2020).

[27] A. Chiesa, E. Macaluso, P. Santini, S. Carretta, and E. Pavarini, First-principles many-body models for electron transport through molecular nanomagnets, Phys. Rev. B **99**, 235145 (2019).

[28] W. H. Appelt, A. Droghetti, L. Chioncel, M. M. Radonjić, E. Muñoz, S. Kirchner, D. Vollhardtd, and I. Rungger, Predicting the conductance of strongly correlated molecules: the Kondo effect in perchlorotriphenylmethyl/Au junctions, Nanoscale **10**, 17738 (2018).

[29] N. Nan, W. Li, P. C. Wang, Y. J. Hu, G. L. Tan, and Y. C. Xiong, Kondo effect and RKKY interaction assisted by magnetic anisotropy in a frustrated magnetic molecular device at zero and finite temperature, Phys. Chem. Chem. Phys. **23**, 5878 (2021).

[30] H. R. Krishna-murthy, J. W. Wilkins, and K. G. Wilson, Renormalization-group approach to the Anderson model of dilute magnetic alloys. I. Static properties for the symmetric case, Phys. Rev. B **21**, 1003 (1980).

[31] R. Bulla, T. A. Costi, and T. Pruschke, Numerical renormalization group method for quantum impurity systems, Rev. Mod. Phys. **80**, 395 (2008).

[32] R. Žitko, and T. Pruschke, Energy resolution and discretization artifacts in the numerical renormalization group, Phys. Rev. B **79**, 085106 (2009).

[33] R. Landauer, Spatial variation of currents and fields due to localized scatterers in metallic conduction, IBM J. Res. Dev. **1**, 223 (1957).

[34] Y. Meir, N. S. Wingreen, and P. A. Lee, Low-temperature transport through a quantum dot: The Anderson model out of equilibrium, Phys. Rev. Lett. **70**, 2601 (1993).

[35] F. B. Anders and A. Schiller, Real-time dynamics in quantum-impurity systems: A time-dependent numerical renormalization-group approach, Phys. Rev. Lett. **95**, 196801 (2005).

[36] J. Steinbauer, S. Biermann, and S. Bhandary, Role of charge transfer in hybridization-induced spin transition in metal-organic molecules, Phys. Rev. B **100**, 245418 (2019).

[37] S. Bhandary, J. M. Tomczak, and A. Valli, Designing a mechanically driven spin-crossover molecular switch via organic embedding, Nanoscale Adv. **3**, 4990 (2021).
[38] Y. Tanaka, N. Kawakami, and A. Oguri, Crossover between two different Kondo couplings in side-coupled double quantum dots, Phys. Rev. B **85**, 155314 (2012).
[39] R. Žitko and J. Bonca, Quantum phase transitions in systems of parallel quantum dots, Phys. Rev. B **76**, 241305(R) (2007).
[40] W.-Z. Wang, Kondo effect and continuous quantum phase transitions in double quantum dots with on-site and interdot repulsion and magnetic field, Phys. Rev. B **83**, 075314 (2011).
[41] J. N. Wang, W. H. Zhou, Y. X. Yan, W. Li, N. Nan, J. Zhang, Y. N. Ma, P. C. Wang, X. R. Ma, S. J. Luo, and Y. C. Xiong, Unified formulations for RKKY interaction, side Kondo behavior, and Fano antiresonance in a hybrid tripartite quantum dot device with filtered density of states, Phys. Rev. B **106**, 035428 (2022).
[42] I. Weymann, Finite-temperature spintronic transport through Kondo quantum dots: Numerical renormalization group study, Phys. Rev. B **83**, 113306 (2011).
[43] P. C. Wang, Y. H. Wang, C. Chen, J. Zhang, W. Li, N. Nan, J. N. Wang, J. T. Yang, A. Laref, and Y. C. Xiong, Frustration-controlled quantum phase transition between multiple singular two-stage Kondo behaviors in a tetrahedral quadruple quantum dot structure, Phys. Rev. B **105**, 075430 (2022).
[44] P. S. Cornaglia and D. R. Grempel, Strongly correlated regimes in a double quantum dot device, Phys. Rev. B **71**, 075305 (2005).
[45] E. V. Anda, G. Chiappe, C. A. Büsser, M. A. Davidovich, G. B. Martins, F. Heidrich-Meisner, and E. Dagotto, Method to study highly correlated nanostructures the logarithmic-discretization embedded-cluster approximation, Phys. Rev. B **78**, 085308 (2008).
[46] R. Žitko, Fano-Kondo effect in side-coupled double quantum dots at finite temperatures and the importance of two-stage Kondo screening, Phys. Rev. B **81**, 115316 (2010).
[47] G.-Y. Yi, C. Jiang, L.-L. Zhang, S.-R. Zhong, H. Chu, and W.-J. Gong, Manipulability of the Kondo effect in a T-shaped triple-quantum-dot structure, Phys. Rev. B **102**, 085418 (2020).
[48] R. Žitko and J. Bonca, Multiple-impurity Anderson model for quantum dots coupled in parallel, Phys. Rev. B **74**, 045312 (2006).
[49] J. R. Schrieffer and P. A. Wolff, Relation between Anderson and Kondo Hamiltonians, Phys. Rev. **149**, 491 (1966).
[50] W. Z. Wang, Spectral properties and quantum phase transitions in parallel triple quantum dots, Phys. Rev. B **76**, 115114 (2007).
[51] P. Gütlich and A. Hauser, Thermal and light-induced spin crossover in iron(II) complexes, Coord. Chem. Rev. **97**, 1 (1990).
[52] P. Gütlich, Y. Garcia, and H. A. Goodwin, Spin crossover phenomena in Fe(II) complexes, Chem. Soc. Rev. **29**, 419 (2000).
[53] K. Kato, M. Takata, Y. Moritomo, A. Nakamoto, and N. Kojima, On-off optical switching of the magnetic and structural properties in a spin-crossover complex, Appl. Phys. Lett. **90**, 201902 (2007).
[54] N. Baadji, M. Piacenza, T. Tugsuz, F. D. Sala, G. Maruccio, and S. Sanvito, Electrostatic spin crossover effect in polar magnetic molecules, Nat. Mater. **8**, 813 (2009).
[55] V. Meded, A. Bagrets, K. Fink, R. Chandrasekar, M. Ruben, F. Evers, A. Bernand-Mantel, J. S. Seldenthuis, A. Beukman, and H. S. J. van der Zant, Electrical control over the Fe(II) spin crossover in a single molecule: Theory and experiment, Phys. Rev. B **83**, 245415 (2011).
[56] T. G. Gopakumar, F. Matino, H. Naggert, A. Bannwarth, F. Tuczek, and R. Berndt, Electron-Induced Spin Crossover of Single Molecules in a Bilayer on Gold, Angew Chem. Int. Ed. **51**, 6262 (2012).
[57] A. Hurley, N. Baadji, and S. Sanvito, Strategy for detection of electrostatic spin-crossover effect in magnetic molecules, Phys. Rev. B **88**, 054409 (2013).
[58] E. J. Devid, P. N. Martinho, M. V. Kamalakar, I. Salitro, U. Prendergast, J.-F. Dayen, V. Meded, T. Lemma, R. González-Prieto, F. Evers, T. E. Keyes, M. Ruben, B. Doudin, and S. J. van der Molen, Spin transition in arrays of gold nanoparticles and spin crossover molecules, ACS Nano **9**, 4496 (2015).
[59] C. Fourmental, S. Mondal, R. Banerjee, A. Bellec, Y. Garreau, A. Coati, C. Chacon, Y. Girard, J. Lagoute, S. Rousset, M.-L. Boillot, T. Mallah, C. Enachescu, C. Barreteau, Y. J. Dappe, A. Smogunov, S. Narasimhan, and V. Repain, Importance of epitaxial strain at a spin-crossover molecule-metal interface, J. Phys. Chem. Lett. **10**, 4103 (2019).
[60] L. Kipgen, M. Bernien, F. Tuczek, and W. Kuch, Spin-crossover molecules on surfaces: From isolated molecules to ultrathin films, Adv. Mater. **33**, 2008141 (2021).
[61] S. K. Kuppusamy, A. Mizuno, A. García-Fuente, S. van der Poel, B. Heinrich, J. Ferrer, H. S. J. van der Zant, and M. Ruben, Spin-crossover in supramolecular Iron(II)-2, 6-bis(1H-Pyrazol-1-yl)pyridine complexes: Toward spin-state switchable single-molecule junctions, ACS Omega **7**, 13654 (2022).
[62] S. Johannsen, S. Ossinger, J. Grunwald, A. Herman, H. Wende, F. Tuczek, M. Gruber, and R. Berndt, Spin crossover in a cobalt complex on Ag(111), Angew. Chem. Int. Ed. **61**, e202115892 (2022).
[63] R. Sánchez-de-Armas, N. Montenegro-Pohlhammer, A. Develioglu, E. Burzurí, and C. J. Calzado, Spin-crossover complexes in nanoscale devices: Main ingredients of the molecule-substrate interactions, Nanoscale **13**, 18702 (2021).
[64] Y. Tong, M. Kelaï, K. Bairagi, V. Repain, J. Lagoute, Y. Girard, S. Rousset, M.-L. Boillot, T. Mallah, C. Enachescu, and A. Bellec, Voltage-induced bistability of single spin-crossover molecules in a two-dimensional monolayer, J. Phys. Chem. Lett. **12**, 11029 (2021).
[65] M. Gavara-Edo, R. Córdoba, F. J. Valverde-Muñoz, J. Herrero-Martín, J. A. Real, and E. Coronado, Electrical sensing of the thermal and light-induced spin transition in robust contactless spin-crossover/graphene hybrid devices, Adv. Mater. **34**, 2202551 (2022).
[66] Y. Zhao, M. Gobbi, L. E. Hueso, and P. Samorì, Molecular approach to engineer two-dimensional devices for CMOS and beyond-CMOS applications, Chem. Rev. **122**, 50 (2022).
[67] A. Dutta, K. Tapio, A. Suma, A. Mostafa, Y. Kanehira, V. Carnevale, G. Bussid, and I. Bald, Molecular states and spin crossover of hemin studied by DNA origami enabled single-molecule surface-enhanced Raman scattering, Nanoscale **14**, 16467 (2022).